TITLE: Transcriptional mediators of treatment resistance in lethal prostate cancer

AUTHORS:

Meng Xiao He	mxhe@g.harvard.edu	1, 2, 3
Michael S. Cuoco	mcuoco@broadinstitute.org	3
Jett Crowdis	jcrowdis@broadinstitute.org	2, 3
Alice Bosma-Moody	abosmamo@broadinstitute.org	2, 3, 4
Zhenwei Zhang	zhenwei_zhang@dfci.harvard.edu	2
Kevin Bi	kevinbi@broadinstitute.org	2, 3
Abhay Kanodia	Abhay.Kanodia@stonybrook.edu	2
Mei-Ju Su	windslove52039@gmail.com	2
Christopher Rodman	crodman5447@gmail.com	3
Laura DelloStritto	laura_Dellostritto@dfci.harvard.edu	2, 9
Parin Shah	parin1308@gmail.com	2
Kelly P. Burke	kelly_Burke@dfci.harvard.edu	2, 5, 6
Benjamin Izar	Bi2175@cumc.columbia.edu	7, 8
Ziad Bakouny	ziad_elbakouny@dfci.harvard.edu	2
Alok K. Tewari	alok_tewari@dfci.harvard.edu	2
David Liu	davidliu@broadinstitute.org	2, 3
Sabrina Y. Camp	scamp@broadinstitute.org	2, 3
Natalie I. Vokes	nvokes@broadinstitute.org	2, 3
Jihye Park	jpark@broadinstitute.org	2, 3
Sébastien Vigneau	Sebastien_Vigneau@dfci.harvard.edu	2, 3, 11
Lawrence Fong	Lawrence.Fong@ucsf.edu	9
Orit Rozenblatt-Rosen	orit@broadinstitute.org	3
Aviv Regev	aregev@broadinstitute.org	3, 10
Asaf Rotem	Asaf_Rotem@dfci.harvard.edu	2, 3, 11
Mary-Ellen Taplin*	Mary_Taplin@dfci.harvard.edu	2
Eliezer M. Van Allen*	EliezerM_VanAllen@dfci.harvard.edu	2, 3, 11

*co-senior authors

AFFILIATIONS:

1. Harvard Graduate Program in Biophysics, Boston, MA
2. Department of Medical Oncology, Dana-Farber Cancer Institute, Boston, MA
3. Broad Institute of Harvard and MIT, Cambridge, MA
4. Harvard Medical School, Boston, MA
5. Department of Immunology, Blavatnik Institute, Harvard Medical School
6. Evergrande Center for Immunologic Diseases, Harvard Medical School and Brigham and Women's Hospital, Boston, MA
7. Columbia Center for Translational Immunology, New York, NY
8. Columbia University Medical Center, Department of Medicine, Division of Hematology/Oncology, New York, NY
9. Division of Hematology and Oncology, University of California, San Francisco, San Francisco, CA
10. Howard Hughes Medical Institute and Koch Institute for Integrative Cancer Research, Department of Biology, MIT, Cambridge, MA
11. Center for Cancer Genomics, Dana-Farber Cancer Institute, Boston, MA

CORRESPONDENCE:
Eliezer M. Van Allen
Dana-Farber Cancer Institute
450 Brookline Ave
Boston, MA 02215
Eliezerm_vanallen@dfci.harvard.edu

ABSTRACT (201 words)

Metastatic castration resistant prostate cancer (mCRPC) is primarily treated with therapies that prevent transcriptional activity of the androgen receptor (AR), cause DNA damage, or prevent cell division. Clinical resistance to these therapies, including second-generation androgen-targeting compounds such as enzalutamide and abiraterone, is nearly universal. Other treatment modalities, including immune checkpoint inhibitors, have provided minimal benefit except in rare subsets of patients[1,2]. Both tumour intrinsic and extrinsic cellular programs contributing to therapeutic resistance remain areas of active investigation. Here we use full-length single-cell RNA-sequencing (scRNA-seq) to identify the transcriptional states of cancer and immune cells in the mCRPC microenvironment. Within cancer cells, we identified transcriptional patterns that mediate a significant proportion of inherited risk for prostate cancer, extensive heterogeneity in *AR* splicing within and between tumours, and vastly divergent regulatory programs between adenocarcinoma and small cell carcinoma. Moreover, upregulation of TGF-β signalling and epithelial-mesenchymal transition (EMT) were both associated with resistance to enzalutamide. We found that some lymph node metastases, but no bone metastases, were heavily infiltrated by dysfunctional $CD8^+$ T cells, including cells undergoing dramatic clonal expansion during enzalutamide treatment. Our findings suggest avenues for rational therapeutic approaches targeting both tumour-intrinsic and immunological pathways to combat resistance to current treatment options.

MAIN (2,745 words)

Despite advances in targeting androgen receptor signalling and other drivers, mCRPC is typically lethal[2]. The identities and proportions of cells within human mCRPC niches is largely unknown. By defining treatment resistant states in human mCRPC, we may reveal biological

drivers that inform new treatment strategies. Thus, we collected fresh biopsies from mCRPC patients from representative metastatic sites for whole exome sequencing, bulk RNA-seq, and scRNA-seq using the Smart-seq2 protocol, which generates full-length transcript sequences[3]. At time of biopsy, patients had experienced varied treatment histories, with approximately even representation before and after treatment with enzalutamide. Smaller proportions of patients had experienced abiraterone, taxanes, and other therapies (Fig. 1a). In addition to adenocarcinomas, one biopsied tumour (09171135) had a small cell carcinoma histology.

After quality control, our cohort consisted of 2,170 deeply sequenced cells from 14 patients and 15 biopsies, including cells from both before and after enzalutamide treatment for one patient (01115655) (Methods; Supplementary Fig. 1a). Following clustering of the single-cell transcriptomes, we manually labelled cell clusters for dominant cell type based on cluster-specific expression of marker genes (Fig. 1b; Methods; Supplementary Table 2). Cancer cells, represented in multiple clusters marked by expression of the adenocarcinoma markers *AR* and *KLK3* (which encodes prostate-specific antigen) or the neuroendocrine marker *CHGA*, were recovered from 12 biopsies, comprising over a third of the cells (n=836). The remainder included cells from the B cell lineage, natural killer (NK) and T cells, monocytes and macrophages, erythroid cells, and neutrophils.

Prostate cancer is highly heritable, with an estimated 57% of variation in risk attributed to inherited variants[4]. Genome wide association studies (GWAS) have not only identified significant risk alleles but also generated results that allow the analysis of even non-significantly associated variants in aggregate to link risk to subsets of the genome. We sought to identify cell types relevant to prostate cancer development by integrating cell-type specific expression patterns from our scRNA-seq data with results from a recent large-scale GWAS of prostate

cancer risk[5]. Using LD score regression applied to specifically expressed genes (LDSC-SEG), we identified significant enrichment of germline heritability for prostate cancer in genomic intervals near genes that were specifically expressed in cancer cells (q = 0.031, Benjamini-Hochberg) (Fig. 1c; Methods)[6]. No significant enrichment was observed for any other cell type, indicating that when assessed during advanced disease, inherited risk for prostate cancer is primarily mediated through tumour-intrinsic mechanisms.

Complex androgen receptor splicing

We therefore assessed transcriptional programs in cancer cells across metastatic niches and clinical contexts. As prostate adenocarcinomas are dependent on androgen signalling for survival, significant attention has been focused on the description and detection of a diverse set of *AR* splice variants. The AR protein contains a DNA-binding domain with transcriptional regulatory activity and a ligand-binding domain required for control of its activity by androgens. Splice variants that omit the ligand-binding domain, particularly AR-V7, have been hypothesized to constitutively activate downstream transcriptional programs independent of androgen binding, providing a resistance mechanism to second generation androgen-targeting therapies[7,8]. Taking advantage of our dataset's even sequencing coverage along transcripts, we detected the presence of specific *AR* splice variants. First, we curated a transcriptome annotation of literature described isoforms (Methods). Then, we remapped all reads from individual cancer cells initially mapping to the *AR* locus, counting the number of reads that uniquely map to individual isoforms (Fig. 2a; Methods). We detected isoform-informative reads indicating the presence of many previously described splice variants within our clinical biopsies, with AR-45, AR-V7, and AR-V12 being uniquely identified in the most cells. AR-45 was detected in every biopsy with any isoform-specific reads. AR-V7 was present in biopsies from both before and after enzalutamide exposure.

Strikingly, we detected multiple *AR* splice variants within the same biopsy and even within the same cell, highlighting the complexity of *AR* splicing in mCRPC.

Isoform-informative reads comprise only a small fraction of reads mapping to any gene, and *AR* splice variants described in literature may not represent a complete census of all isoforms expressed *in vivo* (Supplementary Fig. 2). Therefore, we defined two alternative summary measures of *AR* splicing that permitted characterization within more of the individual cancer cells. *AR* intron 3 contains many of the terminal cryptic/alternative exons included in truncated *AR* isoforms lacking the ligand-binding domain, including AR-V7[7]. We quantified the proportion of total *AR* coverage that lies in intron 3 or in a larger interval that includes intron 3 and upstream exons, which encode the DNA-binding domain (Fig. 2b). Again, we detected significant variation between cancer cells within the same biopsy. Moreover, we detected a clear increase in both measures after enzalutamide treatment for patient 01115655, suggesting decreased transcription of full-length *AR* compared to truncating variants after treatment (Fig. 2c,d). Overall, *AR* splicing patterns in mCRPC cells were highly heterogeneous between and within tumours regardless of treatment resistance state.

Enzalutamide resistance programs

Resistance to second generation androgen-targeting therapies poses a major clinical challenge, and previous work based on bulk whole exome and transcriptome sequencing have identified alterations in *RB1*, *TP53*, and *AR* as associated with poor outcomes[9]. Taking advantage of the single-cell resolution of our data, we examined cancer cells in our cohort to identify changes in expression in cells naïve and exposed to enzalutamide, which functions as a competitive inhibitor of AR that prevents nuclear localization and downstream transcriptional regulatory activity within cancer cells[10]. We scored cancer cells for expression of the MSigDB

hallmark gene sets and select literature-derived gene sets, including several reported as mediating resistance mechanisms, such as genes regulated by the glucocorticoid receptor or AR-V7 and genes associated with a neuroendocrine phenotype[11–22] (Methods). Compared to enzalutamide-naïve cells, exposed cells upregulated several MSigDB hallmark gene sets, including for EMT and TGF-β signalling (Fig. 3a,b; Supplementary Table 1). We sought to corroborate these findings in a published cohort of bulk-sequenced mCRPC transcriptomes and found a similar effect for TGF-β signalling upregulation in enzalutamide-exposed lymph node biopsies, although the number of exposed biopsies was small, and the effect was not statistically significant (Fig. 3c)[9]. We could not analyse bone biopsies due to scarcity of post-enzalutamide samples, and EMT scores were confounded with tumour purity, limiting our ability to draw conclusions from bulk sequencing for this specific finding (Supplementary Fig. 3).

Small cell carcinoma regulatory programs

One patient sample within our cohort derived from a small cell carcinoma, a rare aggressive form of prostate cancer that is not responsive to androgen-targeting therapies[23]. As expected, cancer cells from this biopsy differed drastically in their expression programs, with no detectable *AR* expression, strong downregulation of an *AR* regulated gene set, and marked upregulation of a gene set associated with neuroendocrine prostate cancer (Fig. 4a,b; Extended Data Fig. 1)[12,14].

To mitigate overestimating the importance of idiosyncratic gene expression patterns from a single biopsy, we inferred transcriptional regulatory factor regulons using all cancer cells from our cohort and compared the inferred regulon activities between small cell carcinoma and adenocarcinoma cells[24]. Additionally, we scored small cell carcinoma and adenocarcinoma bulk transcriptomes from a published cohort for expression of the gene lists inferred to comprise each

regulatory factor's regulon[9,22] (Methods). Comparing our data and the published cohort, we observed concordant patterns of differential regulon activity between adenocarcinoma and small cell carcinoma (Fig. 4c). Among the transcriptional regulators with decreased activity in small cell carcinoma are *HOXB13*, which mediates *AR* regulatory activity and response to androgens, and *BHLHE40*, previously reported to be regulated by AR[25–27]. Several ETS family transcription factors showed reduced activity in small cell carcinoma, including *ETV1*, which increases prostate adenocarcinoma invasiveness, *EHF*, whose loss confers stem-like features, and *SPDEF*, an AR-regulated transcription factor whose downregulation promotes EMT[28–30]. On the other hand, considering transcriptional regulators with increased regulon expression in small cell carcinoma, we noted the stemness-promoting factors *NANOG* and *SOX2* and the epigenetic regulator *EZH2*, all of which have been reported to promote lineage plasticity and resistance to androgen-targeting therapies[23,31–33]. Among the transcriptional regulators with the most increased activity in small cell carcinoma cells are *E2F1*, which promotes cell cycle progression upon release from RB1 inhibition and is overexpressed in treatment-emergent small cell neuroendocrine prostate cancer and *LHX2*, previously reported in an expression signature of N-myc driven neuroendocrine prostate cancer[34–36]. We also observed increased activity of three transcriptional regulators whose role in small cell carcinoma has not been previously reported: *HOXB5* and *HOXB6*, two homeobox containing transcription factors, and *NR1D2*, a circadian rhythm regulator (Fig. 4c,d)[37]. Thus, even from a single small cell carcinoma case, we recover generalizable patterns of tumour-intrinsic expression differences, implicating both novel regulons and known transcription regulators mediating treatment resistance.

Cytotoxic cell states and dynamics

To provide a therapeutic axis independent of AR signalling and complementing tumour-intrinsic targeting modalities, clinical trials have tested immune checkpoint inhibitors in prostate cancer. While such therapies have yielded major improvements in a variety of solid tumours, responses in advanced prostate cancer have been muted[1,2]. To improve our understanding of the biology underlying this gap, we characterized infiltrating cytotoxic cells in the mCRPC microenvironment. We sub-clustered T and NK cells identified from initial clustering into 6 clusters, including 2 $CD4^+$ T cell populations, 3 largely $CD8^+$ T cell populations, and a population of strongly $CD16^+$ and largely $CD3^-$ cells dominated by NK cells (Fig. 5a; Extended Data Fig. 2a). One population of $CD8^+$ T cells chiefly derived from bone biopsies was marked by expression of *CXCR4*, consistent with reports in mice that *CXCR4* is necessary for localization of $CD8^+$ T cells to the bone marrow and their subsequent survival[38] (Fig. 5b; Extended Data Fig. 2a, 3a). This cluster had minimal expression of the effector molecule *GZMB*, while all three other cytotoxic clusters exhibited *GZMB* expression, albeit to varying degrees (Fig. 5b; Extended Data Fig. 2b). Another $CD8^+$ T cell population, largely derived from lymph node biopsies, was marked by expression of co-inhibitory receptors *PDCD1*, which encodes PD-1, and *HAVCR2*, which encodes TIM-3, along with elevated expression of *TOX*, *TIGIT*, *ICOS*, *FASLG*, and *LAG3* and minimal *TCF7* expression, suggestive of a dysfunctional effector phenotype (Fig. 5b; Extended Data Fig. 2b,e,f). This population exhibited elevated expression of both *ENTPD1* (encoding CD39, a marker of terminally exhausted $CD8^+$ T cells) and *ITGAE* (encoding CD103), whose co-expression identifies infiltrating cytotoxic cells reactive to cancer cells in other human cancers[39,40] (Extended Data Fig. 2c). Both the NK cell-dominant cluster and the remaining cytotoxic T cell cluster, which included $CD8^+$ T cells and likely γδ T cells, were marked by expression of *GNLY* and substantial fractions of cells expressing *CX3CR1* (Fig. 5b; Extended

Data Fig. 2d). Cells expressing *CX3CR1* also highly expressed *GZMB* and *PRF1*, consistent with previous reports that *CX3CR1* marks a $CD8^+$ T cell population with superior cytolytic function corresponding to a more differentiated effector phenotype that has been observed in models of chronic infection and other cancers[41–43]. We did not observe a distinct cluster of *TCF7* and *SLAMF6* dual-expressing progenitor cells previously reported to mediate response to anti-PD-1 therapy in melanoma (Extended Data Fig. 2e,f)[44]. Broadly, these findings demonstrate that prostate cancer metastases are infiltrated by cytotoxic cells with distinct phenotypes, including dysfunctional and effector states relevant to therapy, that may vary based on metastatic site.

Next, we reconstructed T cell receptor (TCR) complementarity-determining region 3 (CDR3) sequences in our scRNA-seq and corresponding bulk RNA-seq data to better understand the clonal dynamics of infiltrating T cells that expand in response to antigen stimulation. Groups of T cells forming part of an expanded clonotype group, indicated by a shared productive CDR3 sequence, were detected in 6 patients. Clonotype groups detected in lymph node metastases were largely comprised of cells from the $CD8^+$ T cell cluster with elevated co-inhibitory receptor expression, while clonotype groups detected in bone metastases were largely comprised of cells from the *CXCR4*-expressing $CD8^+$ T cell cluster with low *GZMB* expression (Fig. 5d). In one bone biopsy (09171144), a large clonotype group was detected that included both cells from the *CXCR4*-expressing cluster and cells with high *CX3CR1* expression, indicating that cells derived from the same progenitor could take on both phenotypes.

From patient 01115655, we collected cells from biopsies taken both before and after treatment with enzalutamide and noted marked changes in the infiltrating T cell populations (Fig. 5c,e). Before treatment, cytotoxic cells formed a minority of infiltrating T cells, which were dominated by a *SELL*-expressing $CD4^+$ T cell population and cells from a $CD4^+$ T regulatory

cell-enriched cluster with elevated *FOXP3* and *CTLA4* expression (Fig. 5c; Extended Data Fig. 2a). Following treatment, the majority of infiltrating T cells were dysfunctional *PDCD1*-expressing $CD8^+$ T cells (Fig. 5c,e). Of note, for the clonotype group with the most cells recovered from this patient, we detected both the corresponding TCRα and TCRβ CDR3 sequences in bulk RNA-seq of biopsies from both timepoints. As inferred from the bulk sequencing data, the clonal fraction increased sharply from ~5% before treatment to ~25% after treatment, making it the largest detected clone (Fig. 5f). All cells of this clonotype group detected in scRNA-seq were part of the *PDCD1*-expressing dysfunctional cluster. Collectively, these observations suggest that $CD8^+$ T cells can mount an aggressive response against cancer cells during enzalutamide treatment but also that they take on a dysfunctional phenotype that may limit sustained efficacy.

Discussion

To overcome limitations in bulk genomic characterization in uncovering cell-type specific contributions to therapeutic resistance in mCRPC, we describe the transcriptomes of individual cells collected from 15 biopsies covering diverse treatment histories, metastatic sites, and histological types. We find that only cancer cell expression significantly explains the sizeable inherited component of prostate cancer risk. Within small cell carcinoma, in addition to recapitulating expression programs promoting lineage plasticity, we identify novel regulators such as *HOXB5*, *HOBX6*, and *NR1D2*, which show dramatically increased activity both in our study and in an external cohort[9,32,33]. For adenocarcinomas, where resistance to second-generation androgen targeting therapies poses a major clinical challenge, significant attention is devoted to *AR* splice variants encoding constitutively active truncated proteins that promote resistance[7,8]. We find that *AR* splicing varies widely across cells within a single biopsy, with

multiple isoforms detectable in individual cells, including those naïve to second-generation androgen targeting therapies. These findings suggest that focused mechanistic understanding of individual isoforms may be insufficient and that additional studies on the overlapping regulatory activity of co-expressed *AR* splice variants are necessary to fully understand their role in therapeutic resistance. More broadly, we identify upregulation of expression programs associated with TGF-β signalling and EMT following exposure to enzalutamide. This is consistent with evidence from pre-clinical models that inhibition of TGF-β signalling promotes reversion of EMT and may sensitize cancer cells to enzalutamide[45,46]. Recent work focused on human mCRPC bone metastases identify tumour associated macrophages as a source of *TGFB1* expression, providing a target cell population for further study and possible therapeutic targeting (Baryawno, N. *et al*. manuscript submitted). Further studies of mCRPC shortly after initiation of enzalutamide may elucidate earlier cellular responses that ultimately precipitate EMT.

Within infiltrating $CD8^+$ T cells, a subset expressed dysfunction markers such as *PDCD1*, and this population included cells that underwent a dramatic clonal expansion within a patient after enzalutamide treatment, suggestive of tumour reactivity. The presence of this cell population may explain why some patients with advanced prostate cancer respond to immune checkpoint inhibition in combination with androgen-targeting therapies[47]. *ENTPD1* (CD39) expression in this population suggests that targeting immunosuppressive adenosine signalling may provide benefit in addition to targeting the PD-1 axis[48]. This population was uncommon in bone biopsies, which instead contained clonally expanded $CD8^+$ T cells with high effector molecule, low exhaustion marker, and *CX3CR1* expression. This cell state has previously been linked in model systems and other cancers to high cytolytic activity but poor proliferative potential and a requirement for CD4 help[41–43]. Similar cells have been reported as being

unresponsive to PD-L1 blockade, potentially explaining the poor performance of immune checkpoint inhibition in mCRPC bone metastases[1,49]. These results highlight the need for additional immunological dissection of mCRPC, where immune checkpoint inhibition has only been indicated for patients with tumour microsatellite instability[1,2]. Importantly, additional investigation should focus on systematic comparisons of bone and lymph node metastases to confirm whether the observed differences in cytotoxic cell infiltration are generalizable. Intriguingly, TGF-β blockade was recently shown to promote response to immune checkpoint inhibition in prostate bone metastases in mice, potentially enabling rational therapeutic combinations to simultaneously act along both androgen and immune axes[50]. Taken together, we report multiple tumour and immune mechanisms across diverse mCRPC metastatic niches that contribute to treatment resistance and provide therapeutic opportunities for this lethal disease.

References

1. Boettcher, A. N. *et al.* Past, Current, and Future of Immunotherapies for Prostate Cancer. *Front. Oncol.* **9**, (2019).
2. Teo, M. Y., Rathkopf, D. E. & Kantoff, P. Treatment of Advanced Prostate Cancer. *Annu. Rev. Med.* **70**, 479–499 (2019).
3. Picelli, S. *et al.* Smart-seq2 for sensitive full-length transcriptome profiling in single cells. *Nat. Methods* **10**, 1096 (2013).
4. Mucci, L. A. *et al.* Familial Risk and Heritability of Cancer Among Twins in Nordic Countries. *JAMA* **315**, 68–76 (2016).
5. Schumacher, F. R. *et al.* Association analyses of more than 140,000 men identify 63 new prostate cancer susceptibility loci. *Nat. Genet.* **50**, 928 (2018).
6. Finucane, H. K. *et al.* Heritability enrichment of specifically expressed genes identifies disease-relevant tissues and cell types. *Nat. Genet.* **50**, 621–629 (2018).
7. Lu, J., der Steen, T. V. & Tindall, D. J. Are androgen receptor variants a substitute for the full-length receptor? *Nat. Rev. Urol.* **12**, 137–144 (2015).
8. Antonarakis, E. S. *et al.* AR-V7 and Resistance to Enzalutamide and Abiraterone in Prostate Cancer. *N. Engl. J. Med.* **371**, 1028–1038 (2014).
9. Abida, W. *et al.* Genomic correlates of clinical outcome in advanced prostate cancer. *Proc. Natl. Acad. Sci. U. S. A.* **116**, 11428–11436 (2019).
10. Tran, C. *et al.* Development of a Second-Generation Antiandrogen for Treatment of Advanced Prostate Cancer. *Science* **324**, 787–790 (2009).
11. Liberzon, A. *et al.* The Molecular Signatures Database Hallmark Gene Set Collection. *Cell Syst.* **1**, 417–425 (2015).

12. Arora, V. K. *et al.* Glucocorticoid Receptor Confers Resistance to Antiandrogens by Bypassing Androgen Receptor Blockade. *Cell* **155**, 1309–1322 (2013).

13. Hwang, J. H. *et al.* CREB5 Promotes Resistance to Androgen-Receptor Antagonists and Androgen Deprivation in Prostate Cancer. *Cell Rep.* **29**, 2355-2370.e6 (2019).

14. Beltran, H. *et al.* Divergent clonal evolution of castration-resistant neuroendocrine prostate cancer. *Nat. Med.* **22**, 298–305 (2016).

15. Li, Y. *et al.* Targeting cellular heterogeneity with CXCR2 blockade for the treatment of therapy-resistant prostate cancer. *Sci. Transl. Med.* **11**, (2019).

16. Yuan, F. *et al.* Molecular determinants for enzalutamide-induced transcription in prostate cancer. *Nucleic Acids Res.* **47**, 10104–10114 (2019).

17. Cato, L. *et al.* ARv7 Represses Tumor-Suppressor Genes in Castration-Resistant Prostate Cancer. *Cancer Cell* **35**, 401-413.e6 (2019).

18. Ragnum, H. B. *et al.* The tumour hypoxia marker pimonidazole reflects a transcriptional programme associated with aggressive prostate cancer. *Br. J. Cancer* **112**, 382–390 (2015).

19. Hu, R. *et al.* Distinct Transcriptional Programs Mediated by the Ligand-Dependent Full-Length Androgen Receptor and Its Splice Variants in Castration-Resistant Prostate Cancer. *Cancer Res.* **72**, 3457–3462 (2012).

20. Ertel, A. *et al.* RB-pathway disruption in breast cancer. *Cell Cycle* **9**, 4153–4163 (2010).

21. Saal, L. H. *et al.* Poor prognosis in carcinoma is associated with a gene expression signature of aberrant PTEN tumor suppressor pathway activity. *Proc. Natl. Acad. Sci.* **104**, 7564–7569 (2007).

22. DeTomaso, D. *et al.* Functional interpretation of single cell similarity maps. *Nat. Commun.* **10**, 1–11 (2019).

314 23. Puca, L., Vlachostergios, P. J. & Beltran, H. Neuroendocrine Differentiation in Prostate
315 Cancer: Emerging Biology, Models, and Therapies. *Cold Spring Harb. Perspect. Med.* **9**,
316 a030593 (2019).
317 24. Aibar, S. *et al.* SCENIC: single-cell regulatory network inference and clustering. *Nat.*
318 *Methods* **14**, 1083–1086 (2017).
319 25. Navarro, H. I. & Goldstein, A. S. HoxB13 mediates AR-V7 activity in prostate cancer. *Proc.*
320 *Natl. Acad. Sci.* **115**, 6528–6529 (2018).
321 26. Norris, J. D. *et al.* The Homeodomain Protein HOXB13 Regulates the Cellular Response to
322 Androgens. *Mol. Cell* **36**, 405–416 (2009).
323 27. Kiss, Z. & Ghosh, P. Abstract 2898: Elucidating the role of
324 BHLHE40/DEC1/SHARP2/STRA13 in prostate cancer. *Cancer Res.* **76**, 2898–2898 (2016).
325 28. Baena, E. *et al.* ETV1 directs androgen metabolism and confers aggressive prostate cancer in
326 targeted mice and patients. *Genes Dev.* **27**, 683–698 (2013).
327 29. Albino, D. *et al.* ESE3/EHF Controls Epithelial Cell Differentiation and Its Loss Leads to
328 Prostate Tumors with Mesenchymal and Stem-like Features. *Cancer Res.* **72**, 2889–2900
329 (2012).
330 30. Tsai, Y.-C. *et al.* Androgen deprivation therapy-induced epithelial-mesenchymal transition of
331 prostate cancer through downregulating SPDEF and activating CCL2. *Biochim. Biophys.*
332 *Acta Mol. Basis Dis.* **1864**, 1717–1727 (2018).
333 31. Borges, G. T. *et al.* Conversion of Prostate Adenocarcinoma to Small Cell Carcinoma-Like
334 by Reprogramming. *J. Cell. Physiol.* **231**, 2040–2047 (2016).
335 32. Ku, S. Y. *et al.* Rb1 and Trp53 cooperate to suppress prostate cancer lineage plasticity,
336 metastasis, and antiandrogen resistance. *Science* **355**, 78–83 (2017).

337 33. Mu, P. *et al.* SOX2 promotes lineage plasticity and antiandrogen resistance in TP53- and
338 RB1-deficient prostate cancer. *Science* **355**, 84–88 (2017).
339 34. Lee, J. K. *et al.* N-Myc Drives Neuroendocrine Prostate Cancer Initiated from Human
340 Prostate Epithelial Cells. *Cancer Cell* **29**, 536–547 (2016).
341 35. Aggarwal, R. R. *et al.* Whole-Genome and Transcriptional Analysis of Treatment-Emergent
342 Small-Cell Neuroendocrine Prostate Cancer Demonstrates Intraclass Heterogeneity. *Mol.*
343 *Cancer Res.* **17**, 1235–1240 (2019).
344 36. Rickman, D. S. *et al.* ERG Cooperates with Androgen Receptor in Regulating Trefoil Factor
345 3 in Prostate Cancer Disease Progression. *Neoplasia N. Y. N* **12**, 1031–1040 (2010).
346 37. Cho, H. *et al.* Regulation of Circadian Behavior and Metabolism by Rev-erbα and Rev-erbβ.
347 *Nature* **485**, 123–127 (2012).
348 38. Goedhart, M. *et al.* CXCR4, but not CXCR3, drives CD8+ T-cell entry into and migration
349 through the murine bone marrow. *Eur. J. Immunol.* **49**, 576–589 (2019).
350 39. Duhen, T. *et al.* Co-expression of CD39 and CD103 identifies tumor-reactive CD8 T cells in
351 human solid tumors. *Nat. Commun.* **9**, 1–13 (2018).
352 40. Gupta, P. K. *et al.* CD39 Expression Identifies Terminally Exhausted CD8+ T Cells. *PLOS*
353 *Pathog.* **11**, e1005177 (2015).
354 41. Zander, R. *et al.* CD4+ T Cell Help Is Required for the Formation of a Cytolytic CD8+ T
355 Cell Subset that Protects against Chronic Infection and Cancer. *Immunity* **51**, 1028-1042.e4
356 (2019).
357 42. Kanev, K. *et al.* Proliferation-competent Tcf1 CD8 T cells in dysfunctional populations are
358 CD4 T cell help independent. *Proc. Natl. Acad. Sci.* **116**, 20070–20076 (2019).

359 43. Hudson, W. H. *et al.* Proliferating Transitory T Cells with an Effector-like Transcriptional
360 Signature Emerge from PD-1+ Stem-like CD8+ T Cells during Chronic Infection. *Immunity*
361 **51**, 1043-1058.e4 (2019).
362 44. Miller, B. C. *et al.* Subsets of exhausted CD8 + T cells differentially mediate tumor control
363 and respond to checkpoint blockade. *Nat. Immunol.* **20**, 326–336 (2019).
364 45. Paller, C. *et al.* TGF-β receptor I inhibitor enhances response to enzalutamide in a pre-
365 clinical model of advanced prostate cancer. *The Prostate* **79**, 31–43 (2019).
366 46. Song, B. *et al.* Targeting FOXA1-mediated repression of TGF-β signaling suppresses
367 castration-resistant prostate cancer progression. *J. Clin. Invest.* **129**, 569–582.
368 47. Graff, J. N. *et al.* Early evidence of anti-PD-1 activity in enzalutamide-resistant prostate
369 cancer. *Oncotarget* **7**, 52810–52817 (2016).
370 48. Leone, R. D. & Emens, L. A. Targeting adenosine for cancer immunotherapy. *J.*
371 *Immunother. Cancer* **6**, 57 (2018).
372 49. Yamauchi, T., Hoki, T., Odunsi, K. & Ito, F. Identification of dysfunctional CD8+ T-cell
373 subsets rescued by PD-L1 blockade in the tumor microenvironment. *J. Immunol.* **200**, 58.3-
374 58.3 (2018).
375 50. Jiao, S. *et al.* Differences in Tumor Microenvironment Dictate T Helper Lineage Polarization
376 and Response to Immune Checkpoint Therapy. *Cell* **179**, 1177-1190.e13 (2019).

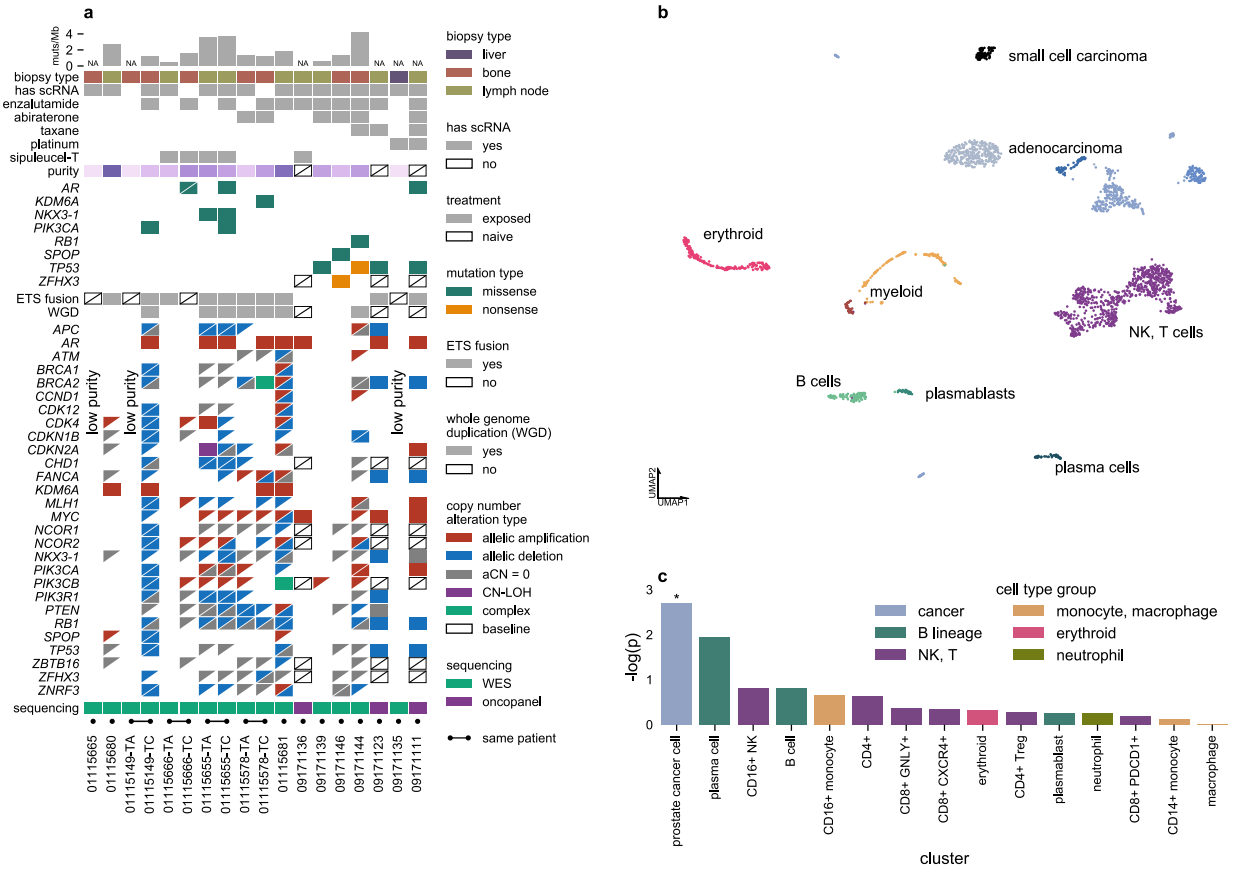

Figure 1. Cellular atlas of mCRPC, identifying heritability for prostate cancer enriched near genes specifically expressed in prostate cancer cells.

a) Summary of clinical and select genomics features of patients and biopsies forming the study cohort. Each column represents a single biopsy. Where available, multiple biopsies from the same patient are displayed in adjacent columns. Patients are identified by numerical prefix, while suffixes after a dash, when present, identify biopsies from the same patient. Boxes with diagonal slashes indicate missing data, e.g. for genes not included in OncoPanel.

b) Projection of single-cell expression onto the first two dimensions of UMAP space. Each dot represents a single cell, and colours correspond to clusters identified by the Louvain algorithm. Clusters are manually labelled with dominant cell type(s) inferred from cluster-specific expression of marker genes.

389 **c)** Enrichment of heritability for prostate cancer near genes specifically expressed in each cell

390 type (compared to cell types in other cell type groups). *: Benjamini-Hochberg FDR < 0.05

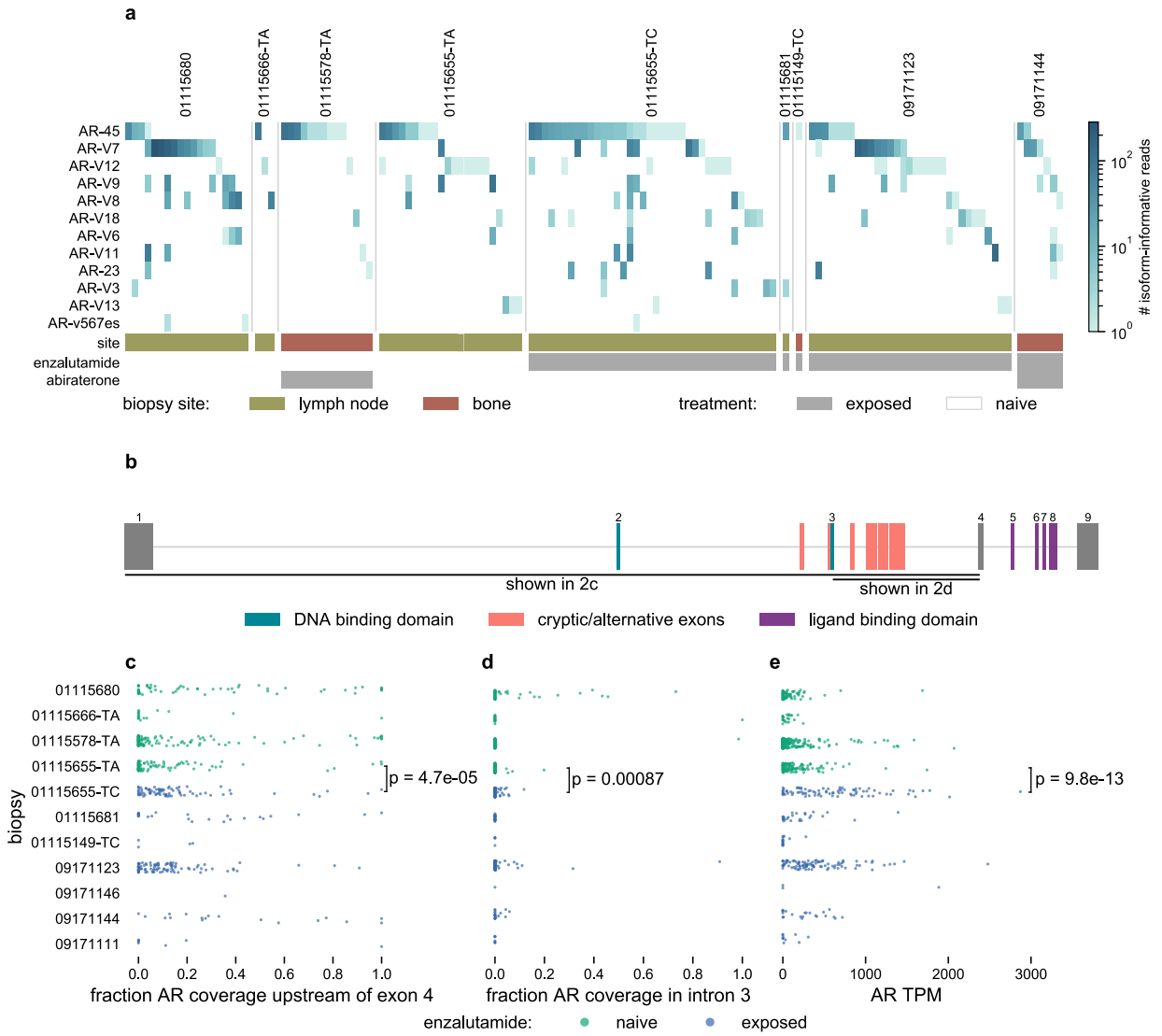

Figure 2. *AR* splicing varies widely across cells within the same tumour and across treatment resistance states.

a) Heatmap displaying number of isoform-informative reads mapping to *AR* variants from single cells. Each column represents *AR* variants detected in a single cell, with only cells that had at least one isoform-informative read shown.

b) Schematic representation of *AR* locus. Rectangles indicate exons. Exons corresponding to the full-length *AR* transcript are numbered, with exons comprising different functional domains coloured. Select alternative exons included in *AR* splice variants are indicated.

c) Fraction of total *AR* coverage upstream of exon 4 (including the DNA-binding domain but excluding the ligand-binding domain) in single cells.

d) Fraction of total *AR* coverage in intron 3 (including multiple cryptic/alternative exons included in truncated splice variants) in single cells.

e) Total *AR* expression in single cells.

c, d, e) *P* value compares cells before (n = 112) and after (n = 83) enzalutamide treatment for patient 01115655 (two-sided Mann-Whitney *U* test).

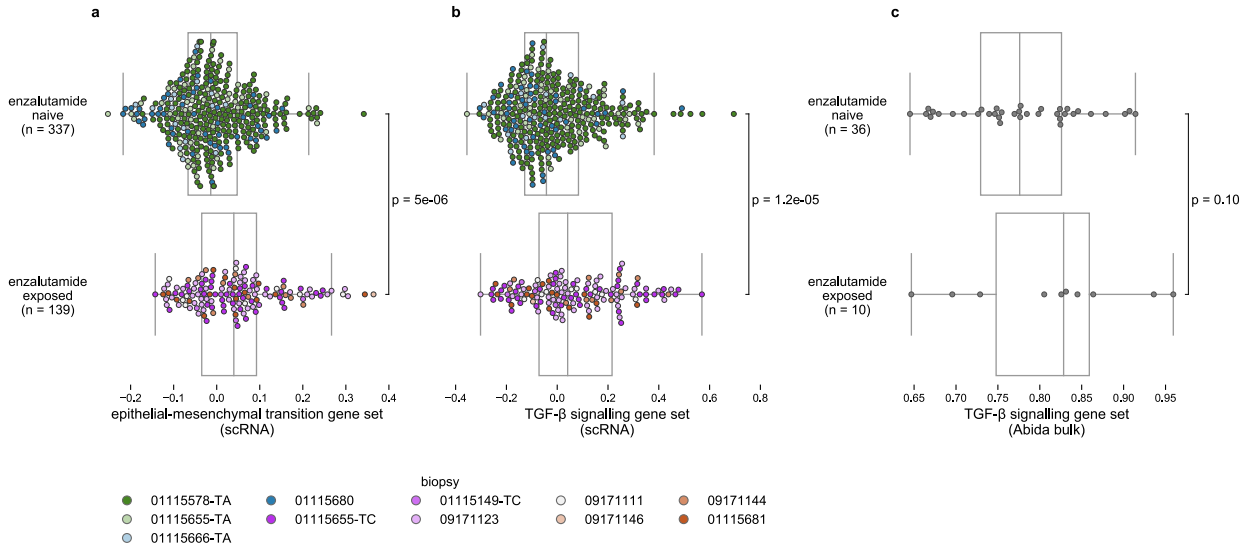

Figure 3. Enzalutamide-exposed adenocarcinoma cells upregulate expression programs associated with epithelial-mesenchymal transition and TGF-β signalling.

a, b) Hallmark epithelial-mesenchymal transition and TGF-β signalling gene set expression scores for individual cells collected before and after enzalutamide treatment. Each dot represents a single cell and is coloured corresponding to biopsy. *P* values from two-sided Mann-Whitney *U* test.

c) Hallmark TGF-β signalling gene set expression scores for bulk RNA-seq of prostate adenocarcinoma lymph node biopsies[9] collected before and after enzalutamide treatment. Each dot represents a single tumour. *P* value from one-sided Mann-Whitney *U* test.

Boxplots: centre line: median; box limits: upper and lower quartiles; whiskers extend at most 1.5x interquartile range past upper and lower quartiles.

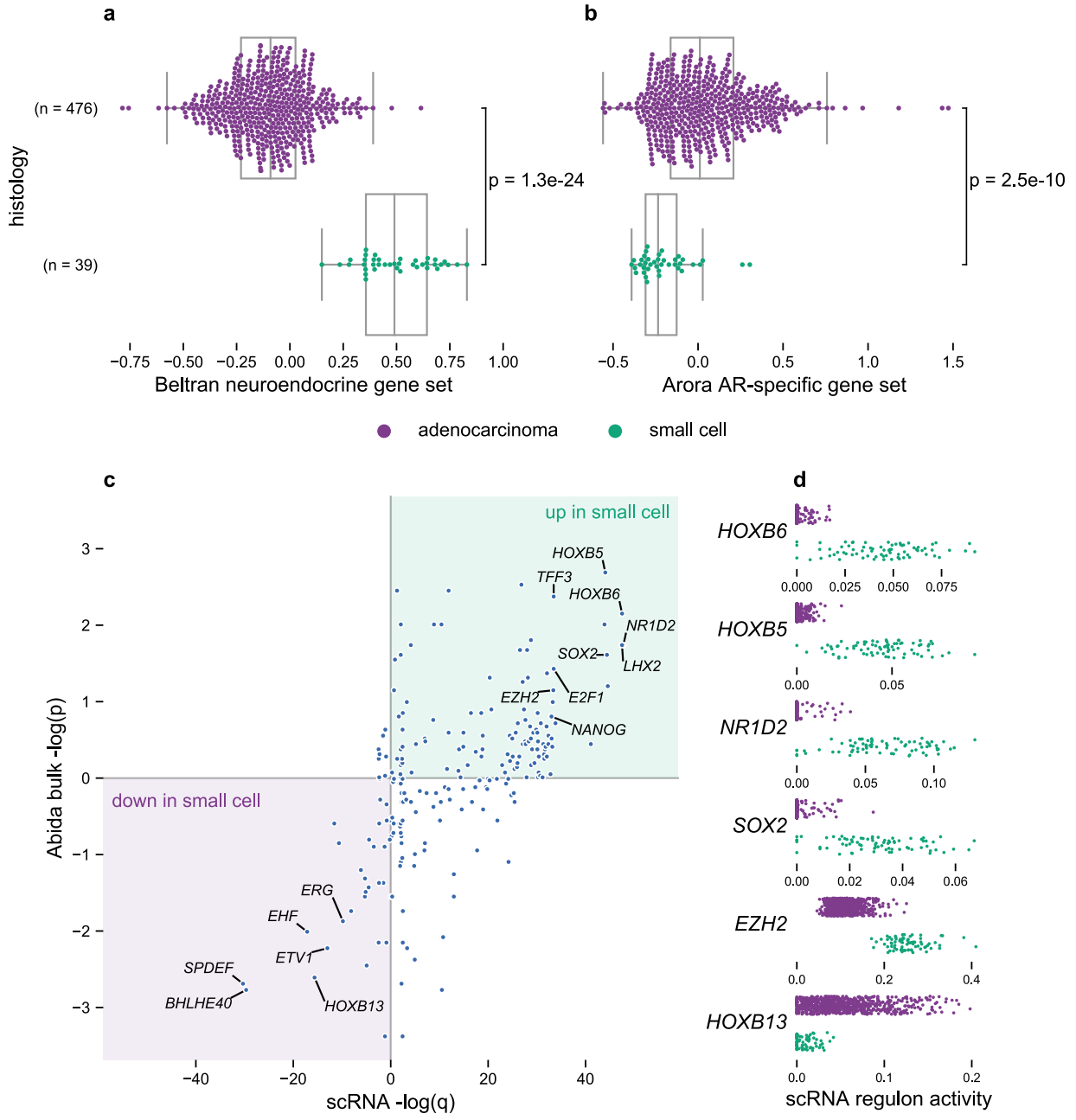

Figure 4. Cancer cells from small cell carcinoma are dominated by distinct regulons compared to adenocarcinoma cells.

a, b) Gene set expression scores in single cells using an expression signature of neuroendocrine prostate cancer[14] and of a set of genes under regulation by *AR*[12]. Boxplots: centre line: median;

box limits: upper and lower quartiles; whiskers extend at most 1.5x interquartile range past upper and lower quartiles.

c) Inferred activity of regulons of different transcriptional regulators. x-axis: *q*-values from comparison of inferred regulon activity in cancer cells from small cell carcinoma (n = 76) vs cancer cells from adenocarcinomas (n = 188, sampled as described in Methods) (negative values indicate regulon is less active in small cell carcinoma; two-sided Mann-Whitney *U* test, median outcome of sampling iterations (Methods) with Bonferroni FWER correction). y-axis: *P* values (two-sided Mann-Whitney *U* test, signed as previous) from comparison of expression scores of scRNA-inferred regulons in bulk RNA-seq of small cell carcinomas (n = 8) vs adenocarcinomas (n = 18) from a published cohort[9].

d) Regulon activity in single cells for select transcriptional regulators.

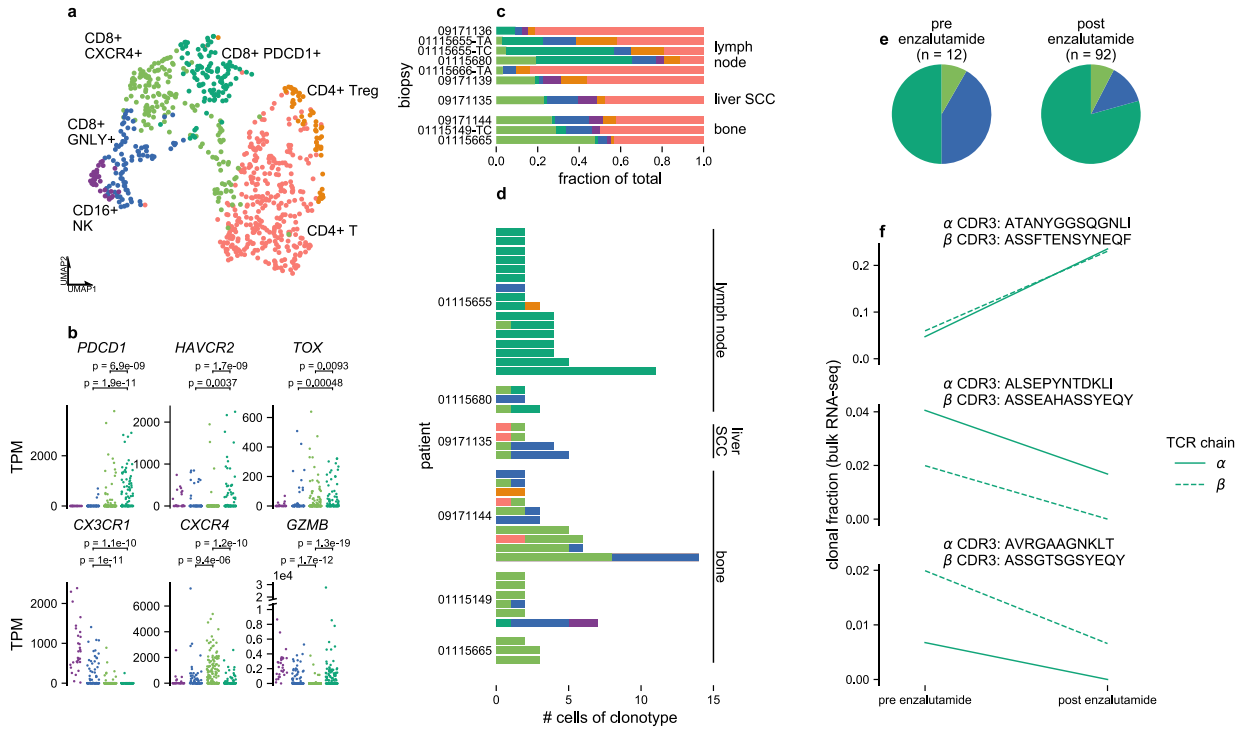

Figure 5. Clonally expanded cytotoxic lymphocytes have different effector phenotypes in distinct metastatic niches.

a) Sub-clustering of NK and T cells. Each dot represents a single cell projected onto UMAP space coloured corresponding to clustering via the Louvain algorithm. Clusters are manually labelled with dominant phenotype/cell type from patterns of marker gene expression. Cluster colours are used throughout subpanels.

b) Expression of select marker, effector, and co-inhibitory receptor genes within cytotoxic clusters, CD16^{+} NK (n = 30), *CD8*$^{+}$ *GNLY*$^{+}$ (n = 84), *CD8*$^{+}$ *CXCR4*$^{+}$ (n = 157), and *CD8*$^{+}$ *PDCD1*$^{+}$ (n = 106). *P* values from two-sided Mann Whitney *U* test.

c) Proportions of cellular phenotypes from each biopsy, grouped by metastatic site, for all biopsies from which high-quality T and NK cells were recovered.

d) T cell clonotypes from TCR reconstruction. Each bar represents cells sharing a reconstructed productive TCR CDR3 sequence and are grouped by patient. Colours indicate phenotype/cell type.

e) Proportions of cytotoxic cell phenotypes in patient 01115655 before and after enzalutamide treatment.

f) Changes in clonal fractions of cytotoxic T cell clonotypes in patient 01115655 following enzalutamide treatment. Each subplot corresponds to a single clonotype with TCRα and β CDR3 amino acid sequences inferred from single-cell RNA-seq. Clonal fractions for the same CDR3 sequences (matching at both nucleotide and amino acid level) inferred from TCR reconstruction in bulk RNA-seq are plotted. All detected single cells of the displayed clonotypes come from the *PDCD1*-expressing $CD8^+$ T cell cluster.

METHODS (2,578 words)

Reference versions

We used human genome reference b37 and the GENCODE[51] release 30 gene annotation lifted over to GRCh37.

Statistical software

Statistical tests were conducted with SciPy[52] v1.3.2 running on Python 3.7. R packages were run on R v3.5.1.

Whole exome analyses

For biopsies with paired tumour and normal samples available, we performed whole exome sequencing with a customized version of a previously described protocol[53]. After DNA shearing, hybridization and exome capture were performed using Illumina's Rapid Capture Exome Kit (with the exception of the normal sample for 01115149 and the tumour sample for biopsy 01115149-TA, which used the Agilent SureSelect Human All Exon 44Mb v2.0 bait set[54]). Libraries were sequenced with 76 bp paired-end reads on an Illumina instrument.

Reads were aligned using BWA[55] v0.5.9 and somatic mutations called using a customized version of the Getz Lab CGA WES Characterization pipeline (https://portal.firecloud.org/#methods/getzlab/CGA_WES_Characterization_Pipeline_v0.1_Dec2018/) developed at the Broad Institute. Briefly, we used ContEst[56] to estimate contamination, MuTect[57] and Strelka[58] to call SNVs and indels, DeTiN[59] to estimate tumour-in-normal contamination, and Orientation Bias Filter[60] and MAFPoNFilter[61] to filter sequencing artefacts. Variants were annotated using VEP[62], Oncotator[63], and vcf2maf v1.6.17 (https://github.com/mskcc/vcf2maf). Copy number alterations, purity, ploidy, and whole genome

doubling status were called using FACETS[64] v0.5.14. Copy number alterations were evaluated with respect to whole genome doubling status.

OncoPanel

For biopsies where whole exome sequencing failed, somatic mutation calls, copy number alterations, and ETS fusion status were taken from OncoPanel, a clinical panel sequencing test available at DFCI[65].

Sample collection and dissociation for single-cell RNA-seq

Tumour samples were collected and transported in Dulbecco's Modified Eagle Medium, high glucose, pyruvate ("DMEM", ThermoFisher Scientific, #11995073) on ice. Single-cell suspensions for single-cell RNA-seq were obtained from tumour core needle biopsies through mechanical and enzymatic dissociation. Samples were first cut into pieces smaller than 1 mm^3 using a scalpel. For bone biopsies, soft tissue was also scraped from the hard bone surface using a scalpel blade. Samples were then dissociated using one of two protocols, chiefly to optimize for yield of viable cells from different metastatic sites. Cells obtained from the two protocols were comparable, and findings were consistent in sub-analyses of cells processed with the same protocol (Supplementary Fig. 4).

For biopsies, 01115655-TC, 01115666-TA, 01115680, 01115681, 09171111, 09171135, 09171136, and 09171139, the resulting tissue fragments were incubated in 3 mL Accumax (Innovative Cell Technologies, #AM105) for 10 min at room temperature on a rocking shaker ("ACC" protocol). Cell suspensions were then filtered with a 100 µm cell strainer (ThermoFisher Scientific #08-771-19) and spun at 580 g for 5 min at 4°C. In cases where cell pellets appeared bloody, red blood cells were lysed with ACK Lysing Buffer (ThermoFisher Scientific, #A1049201) on ice for 1 min, followed by quenching with PBS and an additional centrifugation.

503 The final cell pellet was resuspended in PBS (Fisher Scientific, #MT21040CV) with 2% FBS
504 (Gemini Bio-Products, #100-106).

505 For biopsies 01115655-TA, 01115665, 01115149-TC, 01115578-TA, 09171123,
506 09171144, and 09171146, tissue fragments were incubated in 2-3 mL Medium 199, Earle's Salts
507 ("M199", ThermoFisher Scientific, #11150059) with 1 mg/mL Collagenase 4 (Fisher Scientific,
508 #NC9836075), and 10-20 µg/mL DNAse I (StemCell Technologies, #7900) for 5-10 min in a
509 37°C water bath with intermittent mixing, followed by additional mixing and pipetting ("CD"
510 protocol). Cell suspensions were then filtered with a 100 µm cell strainer, spun at 580 g for 5 min
511 at 4°C, and the resulting pellet resuspended in PBS with 2% FBS. The blood clot from biopsy
512 09171144 was processed in a similar manner, with the exception that red blood cells were lysed
513 with ACK Lysing Buffer on ice at 5-minute increments for a total of 15 min. For the bone
514 marrow aspirate from biopsy 09171144, mechanical and enzymatic dissociation were not
515 performed, and red blood cells were lysed with ACK Lysing Buffer on ice at 5-minute
516 increments for a total of 10 min.

517 *Single-cell sorting*

518 Single cell suspensions in PBS with 2% FBS were stained by incubating for 15 minutes
519 at room temperature protected from light with anti-human PTPRC (CD45) monoclonal antibody
520 conjugated to FITC (1:200 dilution, VWR #ABNOMAB12230), anti-human EPCAM antibody
521 conjugated to PE (1:50 dilution, Miltenyi Biotec #130-091-253), and either Calcein-AM (1:200
522 dilution, ThermoFisher Scientific #C3100MP; biopsies 01115655-TA and 01115665), 7-
523 Aminoactinomycin D (7-AAD) (1:200 dilution, ThermoFisher Scientific #A1310; all other
524 biopsies except sample 01115149-TC), or both (sample 01115149-TC). We first sorted cells with
525 biological dimensions (high FSC-A and high SSC-A), selected single cells, and excluded

doublets or triplets (low FSC-W). Next, we sorted live cells (low 7AAD/ high Calcein-AM) that were $CD45^+$ (high FITC, enriching for immune cells), $EPCAM^+$ (high PE, enriching for cancer cells), or double negative (low FITC/low PE, only in biopsy 09171144) (see Supplementary Fig. 5 for example gating). Cell sorting was performed using a BD Biosciences FACSAria cell sorter (IIu or UV) with FACSDiva software. Individual cells were sorted into the wells of 96-well plates with 10 µL TCL buffer (Qiagen, #1070498) with 1% beta-mercaptoethanol (Sigma 63689) per well. Plates were then sealed, vortexed for 10 s, spun at 3,700 rpm for 2 min at 4°C, and frozen on dry ice.

Transcriptome sequencing, alignment, and quantification

Library preparation for bulk RNA-seq was performed using the Illumina TruSeq Stranded mRNA Sample Preparation Kit (except for biopsy 01115149-TA, which was prepared using the unstranded Illumina TruSeq RNA Sample Preparation protocol (Revision A, 2010)). Libraries were sequenced with 101 bp paired-end reads (except biopsy 01115149-TA, which was sequenced with 76bp paired-end reads) on an Illumina instrument.

For scRNA-seq, RNA was captured from single-cell lysates with 2.2x RNAClean SPRI beads (Beckman Coulter Genomics) without the final elution[67]. After air drying and secondary structure denaturation at 72˚C for three minutes, library construction was performed using a slightly customized Smart-seq2 protocol[66] with 21 cycles of PCR for preamplification. cDNA was purified with 0.8x Ampure SPRI beads (Beckman Coulter Genomics) and eluted in 21 µL TE buffer. During tagmentation and PCR amplification, we used 0.2ng of cDNA per cell and one-eighth of the Illumina NexteraXT (Illumina FC-131-1096) reaction volume. Individual cells were sequenced to a mean depth of ~1.5 million 38 bp paired-end reads on an Illumina NextSeq 500 instrument with 75 cycle high output kits (Illumina TG-160-2005).

After adapter trimming with cutadapt[68] v2.2, reads were aligned using STAR aligner[69] v2.7.2b with parameters: `--outFilterMultimapNmax 20 --outFilterMismatchNmax 999 --outFilterMismatchNoverReadLmax 0.04 --alignIntronMin 20 --alignMatesGapMax 1250000 --alignIntronMax 1250000 --chimSegmentMin 12 --chimJunctionOverhangMin 12 --alignSJstitchMismatchNmax 5 -1 5 5 --chimMultimapScoreRange 3 --chimScoreJunctionNonGTAG -4 --chimMultimapNmax 20 --chimNonchimScoreDropMin 10 --peOverlapNbasesMin 12 --peOverlapMMp 0.1 --chimOutJunctionFormat 1`. `sjdbOverhang` was set to 1 less than the untrimmed read length. We used multi-sample 2-pass mapping for all samples from each patient, first mapping all samples (bulk and single-cell transcriptomes), merging the SJ.out.tab files, then running the second pass with the jointly called splice junctions. STAR BAMs were passed into Salmon[70] v0.14.1 to generate gene-level transcript per million (TPM) quantifications with parameters: `--incompatPrior 0.0 --seqBias --gcBias --reduceGCMemory --posBias`. STAR chimeric junctions were supplied to STAR-Fusion[71] v1.7.0 in kickstart mode to call ETS family fusions.

Single-cell quality control and clustering

After removing low quality cells (fewer than 500 or more than 10,000 detected genes, fewer than 50,000 reads, or more than 25% expression from mitochondrial genes), we used Seurat[72] v3.1.0 to perform first-pass clustering using the TPM matrix rescaled to exclude mitochondrial genes. We manually identified and removed a small number of cells with anomalous expression patterns (chiefly co-expression of high levels of haemoglobin with marker genes for non-erythroid cells). Additionally, some cells that did not cluster with erythroid cells (easily identified with dominant haemoglobin expression) nonetheless had low levels of haemoglobin detected, suggestive of contamination from ambient RNA released from lysed erythroid cells. To account for this, we identified genes whose expression was correlated

(Pearson correlation > 0.2) with total haemoglobin expression levels in non-erythroid cells with detectable haemoglobin. This consisted of a small set of genes with known function in erythroid cell development and function: *AHSP*, *GATA1*, *CA1*, *EPB42*, *KLF1*, *SLC4A1*, *CA2*, *GYPA*, *TFR2*, *RHAG*, *FAXDC2*, *RHD*, *ALAS2*, *SPTA1*, and *BLVRB*. To mitigate batch effects driven by different degrees of contaminating ambient erythroid transcripts, we removed these genes, along with the genes encoding haemoglobin subunits, from the expression matrix for all non-erythroid cells.

We repeated the clustering and conducted all downstream analyses with the filtered expression matrix. After joint clustering of all cells (Fig. 1b), we performed sub-clustering on 3 cell subsets: 1) NK and T cells 2) B-lineage cells 3) myeloid cells. We manually labelled clusters by dominant cell identity, as assessed by marker gene expression patterns (Supplementary Table 2). Briefly, cancer cell clusters were identified by expression of *AR*, *KLK3*, or *CHGA*; T cell populations by *CD3D* and *CD3G*; Tregs by *CD4*, *FOXP3,* and *CTLA4*; NK cells by absence of *CD3D* and *CD3G* and expression of *FCGR3A*, *FCGR3B*, and *GZMB*; erythroid cells by *HBA* and *HBB*; neutrophils by *ELANE*, *CEACAM8*, *AZU1*, and *DEFA1*; macrophages by *APOE*, *C1QA*, and *C1QB*; monocytes by *ITGAX*, *CD14*, *FCGR3A*, and *FCGR3B*; B cells by *CD19* and *MS4A1*; plasmablasts by *CD19* and absence of *MS4A1*; and plasma cells by *SDC1* and high expression of immunoglobulin genes. Additionally, we confirmed the identity of cancer cell clusters by matching transcriptome-inferred copy number alteration profiles generated from inferCNV v0.99.7 (https://github.com/broadinstitute/inferCNV) with those obtained from corresponding bulk whole exome sequencing.

Cluster specifically expressed genes and LDSC-SEG

We grouped cell clusters into 'superclusters' of related cell types (Supplementary Table 2) and performed differential expression to identify markers for each cell cluster, omitting cells in the same supercluster. To mitigate uneven representation of cell types, when comparing against any cluster, we subsampled the same number of cells from each other supercluster and used as even representation as possible of the contained clusters. In determining cancer cell markers, we used as even representation as possible of cells from each biopsy while sampling 200 cancer cells total per iteration. For each cluster, we repeated the sampling 500 times. In each sampling, we performed a one-sided Mann Whitney *U* test for differential expression on all genes with at least 1 TPM expression in at least 10% of the cluster's cells. We then selected the top 10% most upregulated genes (lowest median *P* value across samplings) as cluster specifically expressed genes. We used a 100kb interval around genes for heritability partitioning with LDSC-SEG v1.0.1, additionally including an annotation corresponding to all genes and the baseline v1.1 model[6].

AR *isoform-informative reads*

To identify reads that uniquely map to an *AR* splice variant, we generated a FASTA transcriptome annotation of spliced sequences from isoforms described in literature[7,73–79]. We extracted all reads initially mapped by STAR to the *AR* genomic interval X:66753830-67011796 and then remapped them to our *AR* isoform transcriptome, disallowing clipping, multimapping, or chimeric reads, and requiring end-to-end mapping (STAR parameters: `--outFilterMultimapNmax 1 --alignEndsType EndToEnd --alignSoftClipAtReferenceEnds No --outFilterMismatchNmax 999 --outFilterMismatchNoverReadLmax 0.04 --peOverlapNbasesMin 10`). As our *AR* isoform transcriptome corresponded to transcript sequences *after* splicing, we further excluded reads that mapped with gaps corresponding to additional inferred splice events. We reported all reads that mapped uniquely to an isoform with at most 1 mismatch in Figure 2a.

Gene set scoring, regulon activity

For both bulk samples and single cells, we scored the activity of gene sets with VISION[22] v2.0.0. From single cancer cells, we inferred regulons and transcriptional regulatory factor activity with SCENIC[24] v1.1.2.2. In Figure 4, for single cells, we used SCENIC AUC directly as a measure of regulon activity. For Figure 4c, to infer regulon activity in bulk samples, we extracted the gene sets corresponding to regulons from SCENIC and scored bulk samples for activity of the genes sets using VISION.

When comparing VISION scores in cells from biopsies exposed and naïve to treatment with enzalutamide, we included only cells inferred to be in G1 by Seurat to reduce discovery of signals introduced by different proportions of cycling cells between tumours[72]. We restricted our initial analyses to biopsies with at least 10 G1 cancer cells. As we were interested in generalizable patterns of expression change related to enzalutamide exposure, we attempted to filter out signals driven primarily by expression patterns in any single biopsy by undertaking a subsampling procedure. By considering subsets of the data more balanced for representation from different biopsies, we traded reduced power for more robustness. From either class (enzalutamide naïve vs exposed), we sampled up to 20 cells per biopsy to prevent results from being dominated by tumours with many recovered cells. Additionally, across repeated sampling iterations, we omitted each biopsy in turn, instead sampling cells from other biopsies within its class, keeping the total number of cells the same. We performed 501 iterations of sampling for each biopsy being excluded. For each gene set being scored with VISION, we used the sampling with the median effect size as the summary of all iterations. When measuring effect size, we consistently compared one class vs the other (i.e. always exposed relative to naïve) to ensure

consistency in comparisons of direction of effect. We used the corresponding two-sided Mann Whitney *U* test *P* value as the nominal *P* value for the given gene set.

We additionally took the following steps to filter results that appeared to be driven by a single biopsy: for any given biopsy, we compared samplings when cells from the biopsy were held out vs when cells from the biopsy were included. If the proportion of nominally significant results ($P < 0.05$, same direction of effect as the overall median outcome for the given signature) when the biopsy was excluded was less than 80% of the proportion of nominally significant results when the biopsy was included, we considered any overall finding of differential gene set expression as non-robust and did not report it. We reported signatures with FDR <0.05 in Supplementary Table 1[80]. Note that *P* values shown in Figures 3a, 3b, 4a, and 4b are based on all G1 cells and confirmed the findings from this sampling approach.

For comparisons of regulon activity in small cell carcinoma and adenocarcinoma, we took a similar approach, except that in comparing SCENIC AUC scores, we did not restrict to only G1 cells, as the regulons had been inferred with all cancer cells together. As there was one small cell carcinoma biopsy, cells from that biopsy were never selected for omission across samplings.

Bulk RNA-seq analyses of Abida cohort

In Figures 3c and 4c, we compared our findings to bulk RNA-seq data from a published cohort[9]. Clinical annotations and expression quantifications were obtained from the published supplementary materials and from the authors directly. We converted gene expression values from FKPM to TPM for consistency with the rest of our study. As this cohort included samples sequenced at different centres and from different metastatic sites, we further restricted our analyses to avoid batch effects. For Figure 3c, we analysed only samples sequenced via

transcriptome capture at the University of Michigan, as this was the largest identifiably uniformly sequenced subset. For Figure 4c, as the largest number of small cell carcinoma samples were sequenced at Cornell, we included only small cell carcinoma and adenocarcinoma cases from Cornell in our analyses.

TCR reconstruction

We performed TCR reconstruction and clonotype inference from single-cell RNA-seq with TraCeR[81] v0.6.0. We performed TCR reconstruction and estimation of clonal fraction from bulk RNA-seq using MiXCR[82] v3.0.12. TCRs were inferred as detected in both bulk and single-cell RNA-seq if the CDR3 nucleic acid (and therefore amino acid) sequence matched.

673 **Methods References**

674 51. Frankish, A. *et al.* GENCODE reference annotation for the human and mouse genomes.
675 *Nucleic Acids Res.* **47**, D766–D773 (2019).
676 52. Virtanen, P. *et al.* SciPy 1.0: fundamental algorithms for scientific computing in Python. *Nat.*
677 *Methods* 1–12 (2020) doi:10.1038/s41592-019-0686-2.
678 53. Fisher, S. *et al.* A scalable, fully automated process for construction of sequence-ready
679 human exome targeted capture libraries. *Genome Biol.* **12**, R1 (2011).
680 54. Gnirke, A. *et al.* Solution hybrid selection with ultra-long oligonucleotides for massively
681 parallel targeted sequencing. *Nat. Biotechnol.* **27**, 182–189 (2009).
682 55. Li, H. & Durbin, R. Fast and accurate short read alignment with Burrows–Wheeler
683 transform. *Bioinformatics* **25**, 1754–1760 (2009).
684 56. Cibulskis, K. *et al.* ContEst: estimating cross-contamination of human samples in next-
685 generation sequencing data. *Bioinforma. Oxf. Engl.* **27**, 2601–2602 (2011).
686 57. Cibulskis, K. *et al.* Sensitive detection of somatic point mutations in impure and
687 heterogeneous cancer samples. *Nat. Biotechnol.* **31**, 213–219 (2013).
688 58. Saunders, C. T. *et al.* Strelka: accurate somatic small-variant calling from sequenced tumor-
689 normal sample pairs. *Bioinforma. Oxf. Engl.* **28**, 1811–1817 (2012).
690 59. Taylor-Weiner, A. *et al.* DeTiN: overcoming tumor-in-normal contamination. *Nat. Methods*
691 **15**, 531–534 (2018).
692 60. Costello, M. *et al.* Discovery and characterization of artifactual mutations in deep coverage
693 targeted capture sequencing data due to oxidative DNA damage during sample preparation.
694 *Nucleic Acids Res.* **41**, e67 (2013).

695 61. Lawrence, M. S. *et al.* Discovery and saturation analysis of cancer genes across 21 tumour
696 types. *Nature* **505**, 495–501 (2014).
697 62. McLaren, W. *et al.* The Ensembl Variant Effect Predictor. *Genome Biol.* **17**, 122 (2016).
698 63. Ramos, A. H. *et al.* Oncotator: cancer variant annotation tool. *Hum. Mutat.* **36**, E2423-2429
699 (2015).
700 64. Shen, R. & Seshan, V. E. FACETS: allele-specific copy number and clonal heterogeneity
701 analysis tool for high-throughput DNA sequencing. *Nucleic Acids Res.* **44**, e131–e131
702 (2016).
703 65. Garcia, E. P. *et al.* Validation of OncoPanel: A Targeted Next-Generation Sequencing Assay
704 for the Detection of Somatic Variants in Cancer. *Arch. Pathol. Lab. Med.* **141**, 751–758
705 (2017).
706 66. Picelli, S. *et al.* Full-length RNA-seq from single cells using Smart-seq2. *Nat. Protoc.* **9**,
707 171–181 (2014).
708 67. Shalek, A. K. *et al.* Single-cell transcriptomics reveals bimodality in expression and splicing
709 in immune cells. *Nature* **498**, 236–240 (2013).
710 68. Martin, M. Cutadapt removes adapter sequences from high-throughput sequencing reads.
711 *EMBnet.journal* **17**, 10–12 (2011).
712 69. Dobin, A. *et al.* STAR: ultrafast universal RNA-seq aligner. *Bioinformatics* **29**, 15–21
713 (2013).
714 70. Patro, R., Duggal, G., Love, M. I., Irizarry, R. A. & Kingsford, C. Salmon: fast and bias-
715 aware quantification of transcript expression using dual-phase inference. *Nat. Methods* **14**,
716 417–419 (2017).

717 71. Haas, B. J. *et al.* Accuracy assessment of fusion transcript detection via read-mapping and de
718 novo fusion transcript assembly-based methods. *Genome Biol.* **20**, 213 (2019).
719 72. Butler, A., Hoffman, P., Smibert, P., Papalexi, E. & Satija, R. Integrating single-cell
720 transcriptomic data across different conditions, technologies, and species. *Nat. Biotechnol.*
721 **36**, 411–420 (2018).
722 73. Robinson, D. *et al.* Integrative Clinical Genomics of Advanced Prostate Cancer. *Cell* **161**,
723 1215–1228 (2015).
724 74. Hu, R. *et al.* Ligand-independent androgen receptor variants derived from splicing of cryptic
725 exons signify hormone-refractory prostate cancer. *Cancer Res.* **69**, 16–22 (2009).
726 75. Watson, P. A. *et al.* Constitutively active androgen receptor splice variants expressed in
727 castration-resistant prostate cancer require full-length androgen receptor. *Proc. Natl. Acad.*
728 *Sci. U. S. A.* **107**, 16759–16765 (2010).
729 76. Lu, C. & Luo, J. Decoding the androgen receptor splice variants. *Transl. Androl. Urol.* **2**,
730 178–186 (2013).
731 77. Hu, D. G. *et al.* Identification of androgen receptor splice variant transcripts in breast cancer
732 cell lines and human tissues. *Horm. Cancer* **5**, 61–71 (2014).
733 78. Hu, R., Isaacs, W. B. & Luo, J. A snapshot of the expression signature of androgen receptor
734 splicing variants and their distinctive transcriptional activities. *The Prostate* **71**, 1656–1667
735 (2011).
736 79. Sun, S. *et al.* Castration resistance in human prostate cancer is conferred by a frequently
737 occurring androgen receptor splice variant. *J. Clin. Invest.* **120**, 2715–2730 (2010).

738 80. Benjamini, Y. & Hochberg, Y. Controlling the False Discovery Rate: A Practical and
739 Powerful Approach to Multiple Testing. *J. R. Stat. Soc. Ser. B Methodol.* **57**, 289–300
740 (1995).
741 81. Stubbington, M. J. T. *et al.* T cell fate and clonality inference from single-cell transcriptomes.
742 *Nat. Methods* **13**, 329–332 (2016).
743 82. Bolotin, D. A. *et al.* MiXCR: software for comprehensive adaptive immunity profiling. *Nat.*
744 *Methods* **12**, 380–381 (2015).

ACKNOWLEDGEMENTS

We thank the patients who participated in this study. This work was supported by the National Science Foundation (GRFP DGE1144152 (M.X.H.)), the National Institutes of Health (T32 GM008313 (M.X.H.), T32 CA009172 (A.K.T), K08 CA234458 (D.L.), K08 CA222663 (B.I.), R01 CA227388 (E.M.V.A), and U01CA233100 (L.F. and E.M.V.A.)), a Burroughs Wellcome Fund Career Award for Medical Scientists (B.I.), the Conquer Cancer Foundation (D.L.), the Society for Immunotherapy of Cancers (D.L.), the Prostate Cancer Foundation (L.F.), a Mark Foundation Emerging Leader Award (E.M.V.A.), a Dana-Farber Medical Oncology Translational grant (A. Rotem and E.M.V.A.), and a PCF-V Foundation Challenge Award (E.M.V.A.). Any opinions, findings, and conclusions or recommendations expressed in this material are those of the authors and do not necessarily reflect the views of the National Science Foundation.

AUTHOR CONTRIBUTIONS

M.X.H., A. Rotem, A. Regev, M.-E.T., and E.M.V.A. conceived and designed the overall study. M.S.C., A.K., M.-J.S., and C.R. processed the samples and prepared libraries for scRNA-seq. L.D., J.P., A. Rotem, and O.R.-R. supervised and organized the sample collection and preparation. P.S., B.I., and A. Rotem developed the tissue dissociation protocols. Z.Z., L.D., Z.B., and A.K.T. collected the clinical information. M.X.H. and J.C. analysed the bulk exome sequencing data. M.X.H. performed the heritability enrichment analysis. M.X.H. and A.B.-M. analysed *AR* splicing. M.X.H., D.L., and N.I.K. contributed to the analysis of enzalutamide resistance. M.X.H. and K.B. performed the single-cell regulon analyses. M.X.H., K.B., and K.P.B. analysed the immune cells. M.X.H., L.F., M.-E.T., and E.M.V.A. interpreted the data.

M.X.H., S.V., and E.M.V.A. wrote the manuscript. All authors reviewed and approved the final manuscript.

COMPETING INTERESTS

Z.B. reports research support from Bristol-Meyers Squibb (BMS) unrelated to the current study. D.L. reports funding by a postdoctoral fellowship from the Society for Immunotherapy of Cancers, which is funded in part by an educational grant from BMS. BMS has had no input into the conception, conduct or reporting of the submitted work. L.F. reports receiving commercial research grants from AbbVie, Bavarian Nordic, BMS, Dendreon, Janssen, Merck, and Roche/Genentech. A. Rotem is a scientific advisory board (SAB) member of NucleAI and equity holder in Celsius Therapeutics. A. Regev is a SAB member of Thermo Fisher Scientific and Syros Pharmaceuticals and is a cofounder of and equity holder in Celsius Therapeutics. M.-E.T. has been a paid consultant/advisor to Tokai, Janssen, Medivation, Incyte, and Clovis; and has received advisory board honoraria and trial institutional support from Tokai Pharmaceuticals. E.M.V.A. reports advisory relationships and consulting with Tango Therapeutics, Genome Medical, Invitae, Illumina, Ervaxx, and Janssen; research support from Novartis and BMS; equity in Tango Therapeutics, Genome Medical, Syapse, and Ervaxx; and travel reimbursement from Roche and Genentech, outside the submitted work.

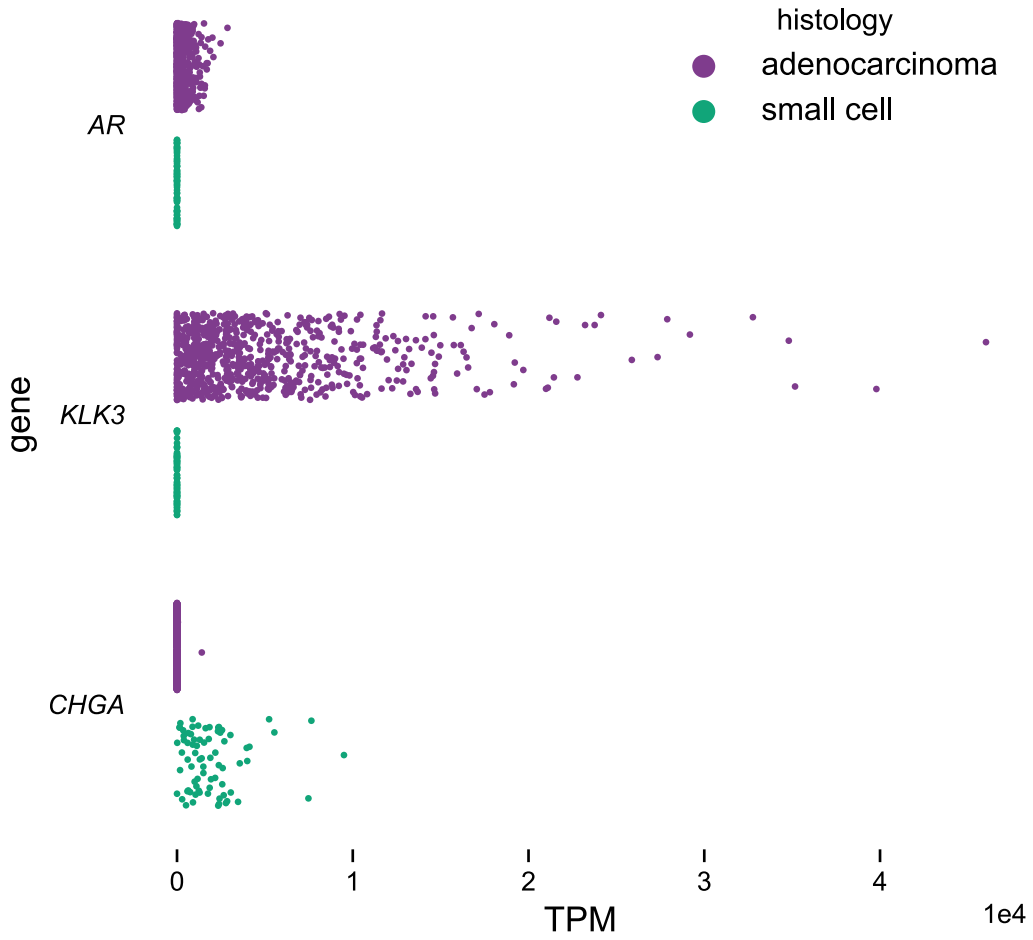

784

785 **Extended Data Figure 1.** Adenocarcinoma and small cell carcinoma cells are clearly

786 distinguished by marker genes.

787 *AR* and *KLK3* (which encodes PSA) expression marks adenocarcinoma cells (n = 760), while

788 *CHGA* marks small cell carcinoma cells (n = 76).

789

790 **Extended Data Figure 2.** Marker gene expression in NK and T cells.

791 Darker colours indicate higher expression of **a)** cell type markers, **b)** dysfunction and activation

792 markers, **c)** markers of tumour-reactive cytotoxic cells, **d)** genes expressed in a *GNLY*-positive

cytotoxic subset, and **e)** genes reported to mark a progenitor population necessary for response after anti-PD-1 therapy in melanoma[44]. Cells are projected onto UMAP space as in Fig. 5a. **f)** Scatterplots showing pairwise co-expression of *HAVCR2*, *SLAMF6*, and *TCF7* in $CD8^+$ T cells. Expression values are in TPM. Points are coloured according to cluster membership as in Fig. 5a.

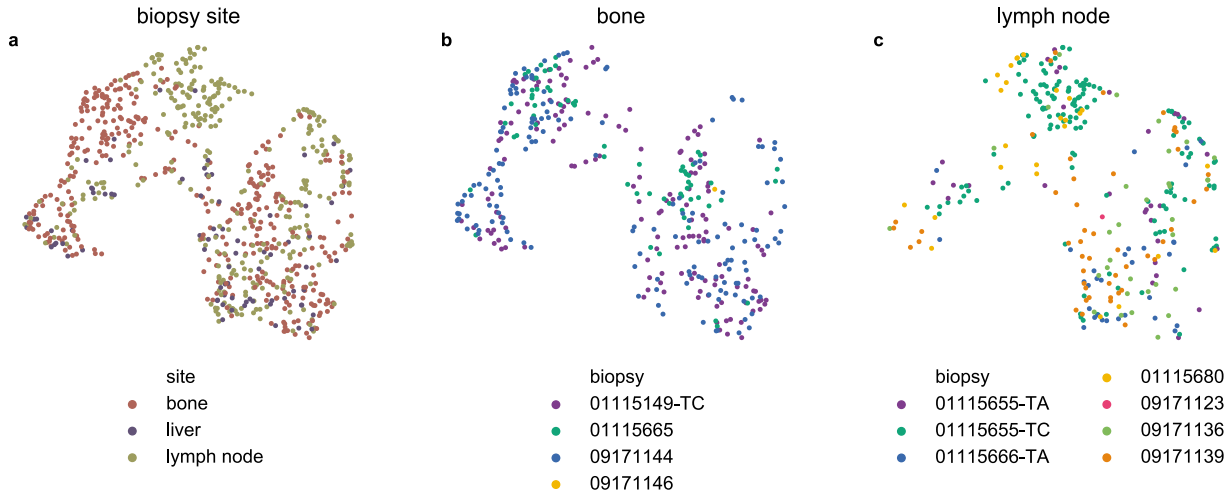

798

799 **Extended Data Figure 3.** Different cytotoxic subsets are represented in different proportions

800 across metastatic sites.

801 NK and T cells are projected onto UMAP space as in Fig. 5a.

802 **a)** Cells are labelled by site of biopsy.

803 Cells infiltrating **b)** bone and **c)** lymph node metastases are labelled by originating biopsy.